The Impact of Misregistration Upon Composited Wide Field of View Satellite Data and Implications for Change Detection

David P. Roy

***Abstract*—Composited wide field of view satellite data are used for many applications and increasingly for studies of global change. Although several compositing schemes have been suggested, all assume perfect geometric registration, which is not operationally feasible. In this study, models of the satellite imaging, geometric registration, and compositing processes are used to investigate the impact of misregistration upon the position of high contrast edges found in composited satellite data. Simulations are performed with respect to the compositing of advanced very high resolution radiometer (AVHRR) and moderate resolution imaging spectroradiometer (MODIS) data. Contrast edges are found to be systematically shifted in maximum and minimum value composites. The degree of shifting increases with the number of orbits that are composited, the degree of misregistration and the view zenith angle. The implications of these findings upon the utility of composited satellite data for change detection are discussed. The shifts may systematically bias estimates of location and area when composited data are used. They may also cause small and/or fragmented features, which are evident in individual orbits to disappear in composited data, precluding the ability to map such features or to detect their occurrence under a change detection scheme.**

***Index Terms*—Change detection, compositing, misregistration.**

I. Introduction

WIDE FIELD of view polar orbiting sensors such as the advanced very high resolution radiometer (AVHRR) and in the future, the moderate resolution imaging spectroradiometer (MODIS), provide near daily sensing of the globe with appropriate resolutions to support global change studies. The utility of their data is reduced however by cloud and atmospheric contamination [1], by changes in the effective spatial resolution across the image swath [2], and by variable sensor response caused by angular sensing and illumination variations combined with the anisotropy of reflectance of most natural surfaces [3] and the atmosphere [4]. Unless these effects are of interest, they should be removed or reduced prior to comparison of different orbits of data. A practical and commonly used approach is to composite multiple orbits into a single data set that ideally is composed of cloud-free, atmospherically clear pixels sensed close to nadir [5]. Composited data are used for many regional and global scale applications including land cover mapping [6], [7], change detection [8], [9], and derivation of biophysical data to parameterize and validate models [10], [11].

Applications utilizing multitemporal, remotely sensed data are dependent on the accurate registration of the data into a common spatial framework. Although previous studies have investigated the impact of misregistration on classification [12] and change detection [13], [14], the impact of misregistration on composited data has not been studied. Spurious differences may be introduced into composited data when the coregistered pixels in different orbits are misregistered merely because the remotely sensed properties at different locations are composited instead of the properties at the same location in each orbit. For example, AVHRR data are commonly composited using the maximum normalized difference vegetation index (NDVI) [5]. Ignoring cloud, atmospheric, and bidirectional reflectance effects, the maximum NDVI compositing procedure will preferentially select at a given location the most vegetated orbit (highest NDVI). When coregistered pixels in different orbits are sensed from different parts of the surface, the maximum NDVI compositing procedure will preferentially select vegetated pixels over spatially adjacent nonvegetated pixels. This may enlarge the boundaries of vegetation features, cause small isolated nonvegetated features to shrink or disappear, and smooth heterogeneous vegetated/nonvegetated scenes. These effects have been observed in maximum NDVI AVHRR composites [15], [16] and reduce their utility for change detection and other applications. This study investigates the impact of misregistration upon the location of high contrast edges found in composited wide field of view satellite data. Such features characterize many static and change/no-change boundaries (e.g., burned/unburned, urban/agriculture, forest/nonforest), and their precise location is required to quantify many change events, particularly those of anthropogenic origin [17]. Rather than examine satellite data empirically, a modeling approach is used so that a range of model parameter values may be investigated that would be difficult to define using satellite data, normalization of temporal variations caused by changing sensing and surface conditions is not required, and the models may be used in a predictive capacity, for example, to model MODIS data which are not yet available.

Compositing procedures are first reviewed followed by illustration of the impact of misregistration on composited AVHRR data. Only compositing procedures that use the maximum or minimum value of some remotely sensed parameter are considered. Models of the satellite imaging, geometric registration, and compositing processes are used to define the probability

Manuscript received May 24, 1999; revised February 17, 2000.

D. P. Roy is with the Department of Geography, University of Maryland, College Park, MD 20742 USA, and also with NASA Goddard Space Flight Center, Greenbelt, MD 20771 USA (e-mail: droy@kratmos.gsfc.nasa.gov).

Publisher Item Identifier S 0196-2892(00)06216-1.

distribution of composited pixel values at fixed locations over a high contrast edge. Shifts in the position of composited contrast edges due to misregistration are derived by comparison of the expected pixel values found when perfectly registered and misregistered orbits are composited. Simulations are performed with respect to the AVHRR and MODIS sensors varying the number of orbits composited, the location and viewing geometry sensed by each orbit, and the degree of misregistration of the different orbits. The implications of the simulation results upon the utility of composited data for change detection are discussed.

II. Overview of Compositing Procedures

Compositing procedures are used widely to produce AVHRR data sets [18], [19] and are used to produce several standard MODIS land products [20]. Compositing is a form of data fusion as defined [21]. Compositing procedures either select from colocated pixels in the different orbits of geometrically registered data the pixel that best satisfies some compositing criteria or combine the different pixel values together. Compositing criteria have included the maximum NDVI, maximum difference in red and near-infrared reflectance, maximum thermal radiance, maximum surface temperature, minimum red reflectance, minimum scan angle, and combinations of these [5], [16], [19], [22]–[24]. Recently, the minimum blue reflectance has been suggested for compositing MODIS and SeaWiFS land surface reflectance data [25]. Compositing criteria have been developed for burned area change detection, including the minimum near-infrared reflectance [26], minimum estimated albedo [27], and the maximum minus the minimum of a burn scar index [28]. Some of the above criteria have been shown to select AVHRR pixels due to anisotropic sensing effects rather than select pixels with reduced cloud and atmospheric contamination [23], [29]. Compositing procedures that model the bidirectional reflectance have been developed to combine all or most of the coregistered pixels sensed over the compositing period to estimate a nadir reflectance [30]. This latter approach is not considered in this study, although it is likely to be sensitive to data misregistration for the reasons discussed in the introduction.

III. Illustration of the Impact of Misregistration on Composited AVHRR Data

The impact of misregistration upon compositing is illustrated using 23 daily NOAA-11 AVHRR local area coverage images (1.1 km pixels) sensed over the Okavango River, Botswana. The images were preprocessed using the Pathfinder II processing chain [19] and were resampled by nearest neighbor resampling with a pixel dimension of 1.1 km. The images were coregistered with no more than one pixel (1.1 km) root mean square error using ground control points and a low order polynomial mapping function.

Fig. 1 illustrates NDVI (left column) and apparent surface temperature (right column) sensed on three separate days. Apparent surface temperature (T_s) was calculated using the split-window technique [31]. The differences in the apparent spatial resolution of these images are caused by differences in their viewing geometry. The August 23 image (middle row) was sensed with the greatest view zenith angles and therefore has the lowest apparent spatial resolution. The NDVI and T_s values are inversely proportional because of factors that include latent heat transfer through evapotranspiration and because of the lower heat capacity and thermal inertia of vegetation compared to that of soil. The Okavango River, running diagonally across each image, is greener and cooler than the surrounding savanna because it is mostly covered by papyrus. The lower part of the September 14 images (bottom row) are partly obscured by a smoke plume caused by local biomass burning.

Fig. 2 illustrates maximum NDVI composites (left column) and maximum T_s composites (right column) made from two, nine, and 23 images. The last images used in each compositing period correspond to the images illustrated on corresponding rows in Fig. 1. As more images are composited, the width of the river becomes smaller in the maximum T_s composites and becomes larger in the maximum NDVI composites. Although the images were coregistered with no more than one pixel root mean square error, there is more than one pixel difference between the width of the river in the September 14 images (Fig. 1, bottom row) and the maximum value composites produced using 23 images sensed from August 15 to September 14 (Fig. 2, bottom row). These figures illustrate how the positions of high contrast edges such as the sides of the Okavango River, may be altered by compositing.

IV. Satellite Imaging and Geometric Registration

A. Satellite Imaging Model

The noise free optical imaging process may be modeled as the convolution of the scene radiance with the sensor point spread function (PSF) [32] defined

$$g(x) = \int_{-\infty}^{\infty} f(\alpha) h(x - \alpha)\, d\alpha \tag{1}$$

where

- $g(x)$ optical image (radiance distribution);
- $f(x)$ scene radiance distribution;
- $h(x)$ sensor point spread function.

The sensor PSF is considered a good measure of an imaging system's performance. An ideal (physically unobtainable) imaging system would have a PSF that causes no smoothing of the scene and can be described by an impulse function $\delta(x)$ defined

$$\delta(x) = 0 \quad \text{when } x \neq 0 \quad \text{and} \quad \lim_{\varepsilon \to 0} \int_{-\varepsilon}^{\varepsilon} \delta(x)\, dx = 1. \tag{2}$$

The sensor optics, detector, electronic filters, and sensor motion are commonly modeled as a single acquisition PSF by convolving the individual PSF's of these effects together [33]. The optical image may then be modeled as the convolution of the scene radiance distribution with the acquisition PSF. The measurement made by a detector will be referred to as an observation and the sensed surface dimensions will be referred to as the observation dimensions. If linear mixing occurs, then the sensed contributions of the scene components are directly proportional

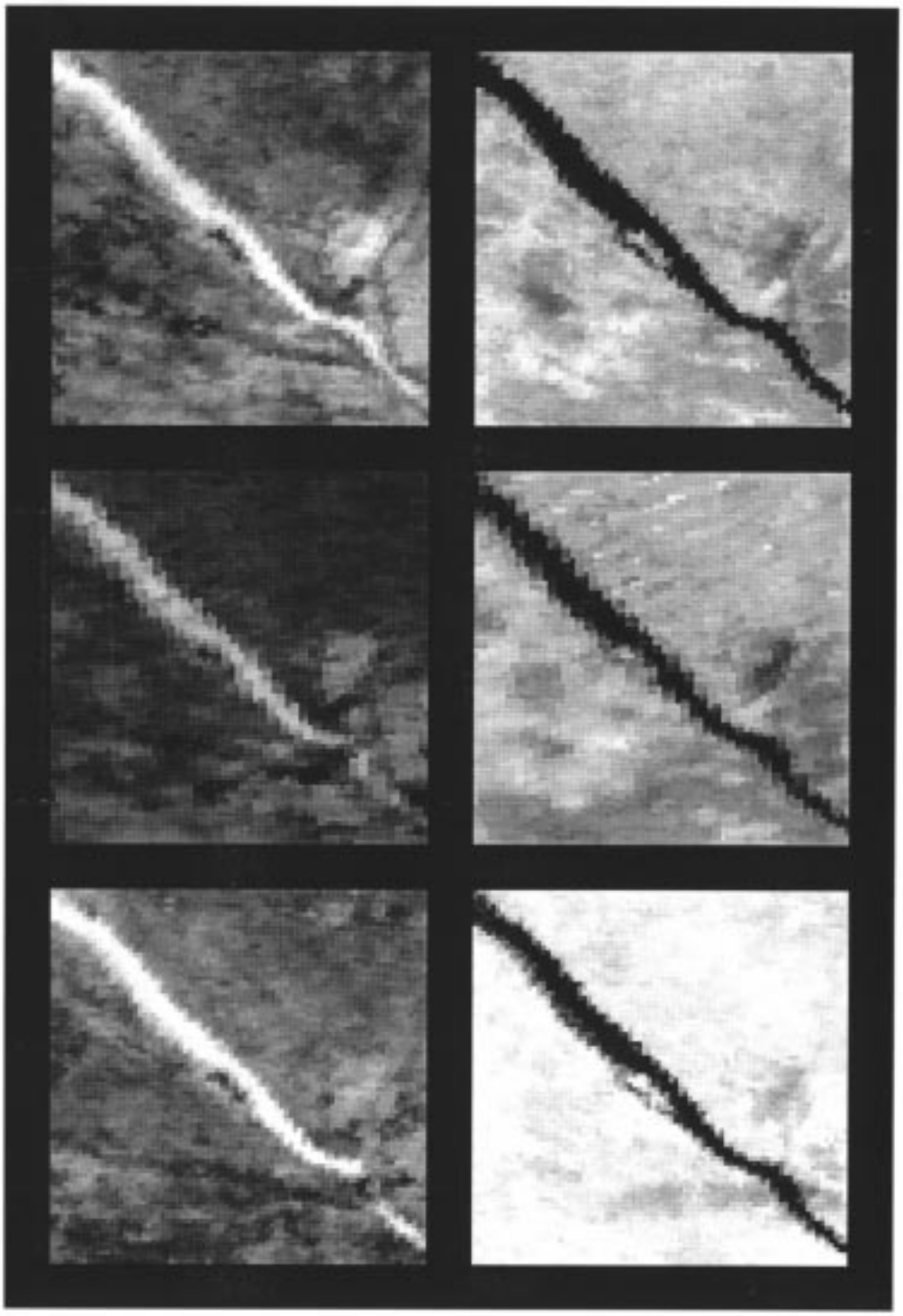

Fig. 1. Three orbits of NDVI (left column) and apparent surface temperature (right column) derived for a common area of 82 × 82 1.1 km AVHRR pixels sensed over the Okavango River, Botswana. The data were sensed on August 16 (top), August 23 (middle), and September 14 (bottom) 1989. The mean view zenith angles for the three orbits are 48° (top), 60° (middle), and 47° (bottom).

to their surface area [34]. To simulate linear mixing, the acquisition PSF is modeled with a flat response over the observation dimension as

$$h(x) = \begin{cases} \dfrac{1}{w}, & |x| \leq \dfrac{w}{2} \\ 0, & \text{otherwise} \end{cases} \tag{3}$$

where $h(x)$ is the acquisition point spread function given linear mixing, and w is the observation dimension in the x axis.The optical image collected at the sensor is digitized and quantized into discrete values for electronic storage and transmission. If the optical image is sampled at constant intervals then the resultant digital image can be expressed as

$$g_s(x) = \sum_{i=-\infty}^{\infty} g(i\Delta x_s + \phi_s)\delta(x - i\Delta x_s - \phi_s) \tag{4}$$

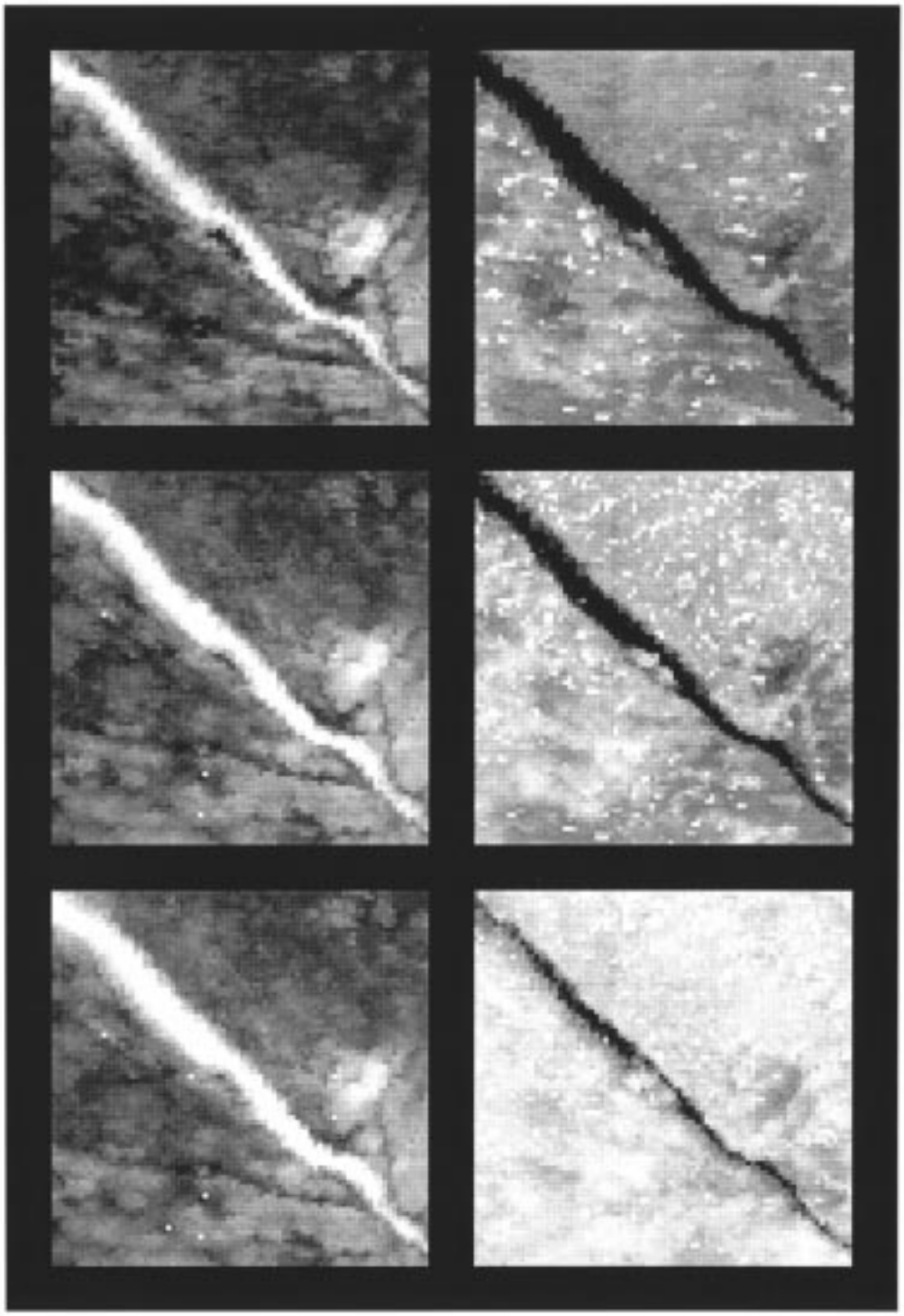

Fig. 2. Three maximum NDVI composites (left column) and three maximum apparent surface temperature composites (right column) produced using two orbits sensed from August 15 to August 16 (top), nine orbits sensed from August 15 to August 23 (middle), and 23 orbits sensed from August 15 to September 14 (bottom). The data sensed over the same region illustrated in Fig. 1.

where

$g_s(x)$ digital image (sampled optical image);
$g(x)$ optical image;
Δx_s sample interval;
ϕ_s sample-scene phase $(0 \leq \phi_s < \Delta x_s)$.

The sample-scene phase describes the position of the samples and the sample interval defines the digital image pixel dimensions relative to some surface coordinate system. Wide field of view whiskbroom sensors such as the AVHRR and MODIS sense the surface using a mirror which rotates at a fixed angular rate around an axis parallel to the along track direction of flight. The optical image is then sampled at a constant temporal rate. This sensing configuration and earth curvature effects cause the AVHRR and MODIS observation dimensions and sample interval to increase along scan at greater view zenith angles [2], [35]. Similarly, the along-track observation dimensions increase

at greater view zenith angles but by less than half the along scan increase. In the along-track direction the sample interval is primarily dependent upon the forward velocity of the sensor and the angular velocity of the scan mirror which are designed to be constant. The AVHRR and MODIS along-track sample interval is approximately constant for the same view zenith angle in consecutive scan lines.

B. Geometric Registration Model

Satellite data production systems conventionally register different orbits of data by geometric correction of each orbit into a common Earth-based coordinate system. Geometric correction can be considered a two-stage process. First, the sensed observations are geolocated, and then they are gridded into a predefined georeferenced grid.

Geolocation may be performed using parametric or nonparametric approaches [36]. Parametric approaches require information concerning the sensing geometry and the sensor exterior orientation parameters (attitude and position) to model the circumstances that produced the sensed data. Terrain relief information is also required to remove relief distortion effects. Nonparametric approaches, such as polynomial warping, require the identification of distinct features that have known locations to model the spatial relationship between the sensed data and an Earth based coordinate system. Conventionally point-like features termed ground control points (GCP's) are used [37], [38]. Satellite geolocation has been performed most accurately using both approaches where models of the sensing geometry, sensor exterior orientation, and the earth are combined with GCP's to reduce model errors and distortions that cannot be modeled e.g., [39].

Gridding may be performed efficiently by mapping the predefined coordinates of the geometrically correct image pixels into the sensed digital image [40]. The geometrically correct image pixel values are then interpolated from the local neighborhood of sensed digital image pixels. This process, known as image resampling, may be conceptualized as sampling from a continuous surface interpolated through the sensed digital image pixel values. The continuous resampled image may be defined [41] as

$$g_r(x) = \sum_{i=-\infty}^{\infty} g_s(i\Delta x_s + \phi_s) r(x - i\Delta x_s - \phi_s) \tag{5}$$

where

$g_r(x)$	resampled image (continuous)
$g_s(x)$	digital image (discrete)
$r(x)$	resampling function
Δx_s	sample interval (sensed digital image pixel dimension)
ϕ_s	sample-scene phase $(0 \leq \phi_s < \Delta x_s)$

Satellite data are usually gridded by nearest neighbor resampling prior to compositing. This is because nearest neighbor resampling is computationally inexpensive and does not alter the sensed digital image values. However, nearest neighbor resampling may introduce one-dimensional geometric shifts up to one half the observation dimension. Nearest neighbor resampling may be defined [42] as

$$r(x) = \begin{cases} 1 & -\dfrac{\Delta x_s}{2} \leq x < \dfrac{\Delta x_s}{2} \\ 0 & \text{otherwise} \end{cases} \tag{6}$$

where $r(x)$ is the nearest neighbor resampling function, and Δx_s is the digital image pixel dimension in the x axis. The geometrically correct image is computed by sampling the continuous resampled image at the centers of each geometrically correct image pixel (7). The geometrically correct pixel dimensions are usually set equal to the nadir observation dimensions and their positions are predefined in a regular grid

$$g_c(x) = \sum_{i=-\infty}^{\infty} g_r(i\Delta x_c + e(x) + \phi_c) \times \delta(x - i\Delta x_c - e(x) - \phi_c) \tag{7}$$

where

$g_c(x)$	geometrically corrected image;
$g_r(x)$	resampled image;
Δx_c	geometrically correct image pixel dimension;
$e(x)$	geolocation error;
ϕ_c	geometrically correct image pixel phase $(0 \leq \phi_c < \Delta x_c)$.

Any geolocation errors will cause the geometrically correct image to be sampled at incorrect locations. Geolocation errors are compounded by resampling artifacts such as nearest neighbor resampling shifts, which together reduce the relative registration accuracy of different orbits of geometrically corrected satellite data.

V. Statistical Model of the Effects of Misregistration Upon the Location of a High Contrast Edge in Composited Wide Field of View Satellite Data

The equations described in Section IV are used to model the imaging and nearest neighbor resampling of an orbit of satellite data sensed over a high contrast edge. Statistical models are developed that describe the probability distribution of a pixel value in a single orbit of geometrically correct data and in a minimum or maximum value composite derived from many orbits of geometrically correct data. Shifts in the position of the composited contrast edge due to misregistration are derived by comparison of the expected pixel values found when perfectly registered and misregistered orbits are composited.

A. Modeling Assumptions

The following assumptions are made for mathematical tractability.

1) The radiometric resolution and calibration of the sensor are sufficient to allow detection of a high contrast edge over many orbits and at different sample-scene phases.
2) The remotely sensed parameter used to composite the data mixes linearly.

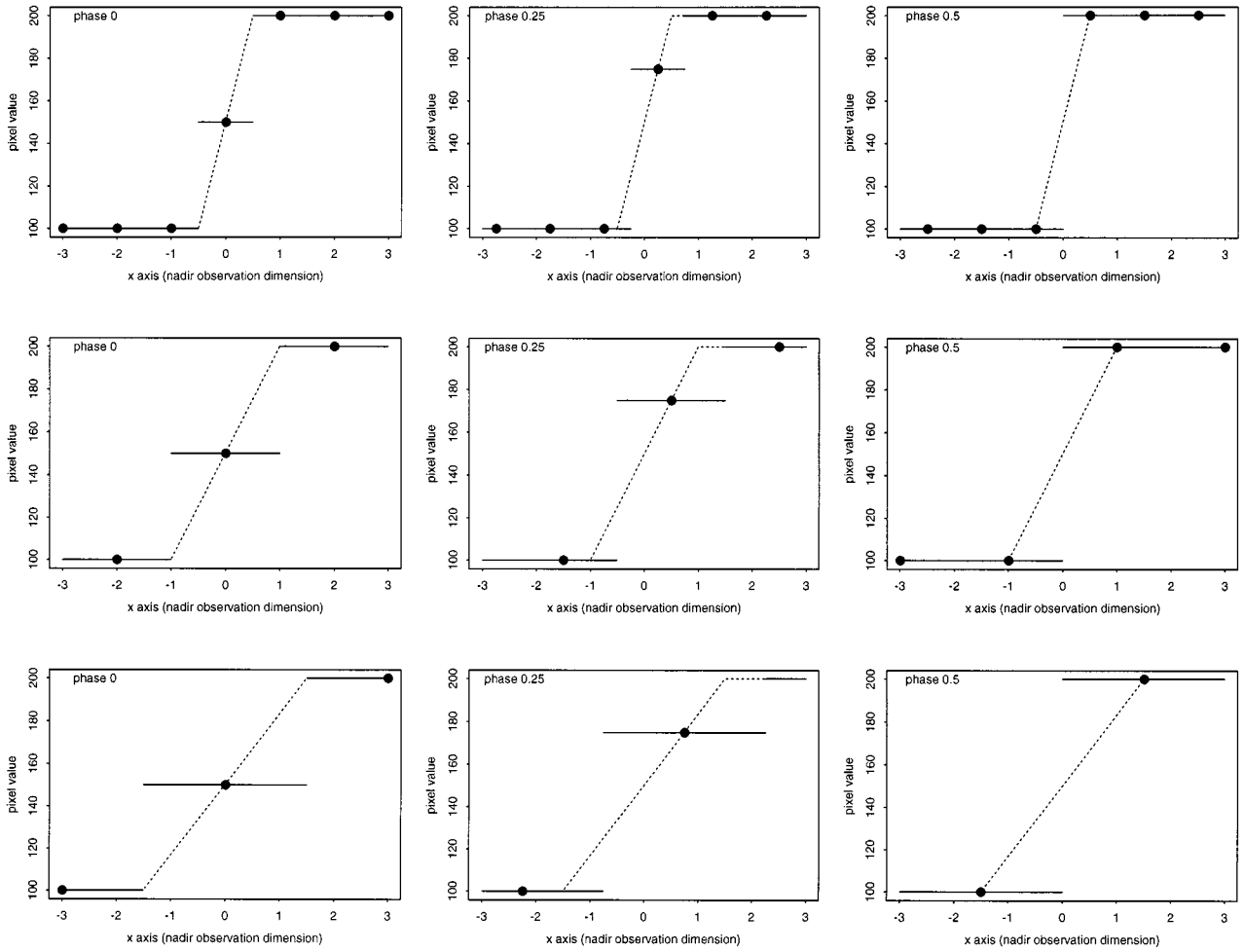

Fig. 3. Optical image assuming linear mixing (dashed line), digital image (dots), and nearest neighbor resampled image (solid lines) of a hypothetical high contrast edge located at $x = 0$ and defined by low ($k1 = 100$) and high ($k2 = 200$) values of some remotely sensed measure. Nadir (top), off-nadir (middle), and far off-nadir (bottom) imaging cases are shown where the sampling interval (digital image pixel dimension) is one, two, and three times the nadir observation dimension, respectively. Sample-scene phases of 0.0, 0.25, and 0.5 the local observation dimension are illustrated.

3) The observations are noise free, cloudless, and uncontaminated by atmospheric effects.
4) Adjacent observation dimensions are non-overlapping and spatially contiguous.
5) The sample interval (sensed digital image pixel dimension) is equal to the local observation dimension, which is assumed to be constant over several adjacent observations.
6) The geolocation errors of different orbits are independent.

These assumptions are not usually met when satellite data are composited. Linear mixing may not occur for certain land cover mixtures (i.e., sparse woodland [43] and when certain thermal parameters are used to composite the data [44]). Satellite data are not noise free and the sensing and sampling geometry are considerably more complex than are modeled here. In particular, adjacent AVHRR and MODIS observation dimensions overlap by varying amounts across the sensor field of view [35], [45]. Furthermore, the geolocation in different orbits may not be independent as sensor exterior orientation parameters may be temporally correlated over periods of many days [45], [46]. For these reasons, the quantitative MODIS and AVHRR simulations results described later in this study should be interpreted with care.

B. Satellite Imaging and Nearest Neighbor Resampling of an Orbit of Data Sensed over a High Contrast Edge

A high contrast edge such as a land–water interface, a soil–vegetation interface, or a burned–unburned vegetation interface is modeled as (8). The feature is defined by low and high values of a remotely sensed parameter used for maximum or minimum value compositing such as, for example, NDVI [5] or blue reflectance [25]

$$f(x) = \begin{cases} k1 & x < 0 \\ k2 & x > 0 \end{cases} \tag{8}$$

where $f(x)$ is the high contrast edge composed of components $k1$ and $k2$ ($k2 > k1$) is defined by some remotely sensed compositing parameter. Given linear mixing the optical image of the contrast edge is defined

$$\begin{aligned} g\left(x \le -\frac{w}{2}\right) &= k1 \\ g\left(-\frac{w}{2} < x < \frac{w}{2}\right) &= \left(\frac{k2-k1}{w}\right)x + \left(\frac{k2+k1}{2}\right) \\ g\left(x \ge \frac{w}{2}\right) &= k2 \end{aligned} \tag{9}$$

where $g(x)$ is the optical image, and w is the observation dimension in the x axis. The nearest neighbor resampled image of the contrast edge is defined (10). Only imaging cases where the observation dimension is equal to or an integer multiple of the nadir observation dimension are modeled

$$\begin{aligned} & g_r\left(x \le z - \frac{\Delta x_s}{2}\right) = k1 \\ & g_r\left(z - \frac{\Delta x_s}{2} < x \le z + \frac{\Delta x_s}{2}\right) \\ & \quad = \left(\frac{k2 - k1}{\Delta x_s}\right) z + \left(\frac{k1 + k2}{2}\right) \\ & g_r\left(x > z + \frac{\Delta x_s}{2}\right) = k2 \\ & z = \phi_s \quad \text{when } 0 \le \phi_s < \frac{\Delta x_s}{2} \\ & z = \phi_s - \Delta x_s \quad \text{otherwise} \end{aligned} \tag{10}$$

where

$g_r(x)$	nearest neighbor resampled image;
ϕ_s	sample-scene phase ($0 \le \phi_s < \Delta x_s$);
Δx_s	sample interval (sensed digital image pixel dimension);
Δx_s	$w_{\text{nadir}} i$;
w_{nadir}	nadir observation dimension;
i	positive integer;
$k1, k2$	values either side of the contrast edge ($k2 > k1$).

The nearest neighbor resampled image is defined by two or three discrete pixel values depending upon the sample-scene phase

$$\begin{aligned} & g_0 = k1 \\ & g_1 = \left(\frac{k2 - k1}{\Delta x_s}\right) z + \left(\frac{k1 + k2}{2}\right) \\ & g_2 = k2 \\ & z = \phi_s \quad \text{when } 0 \le \phi_s < \frac{\Delta x_s}{2} \\ & z = \phi_s - \Delta x_s \quad \text{otherwise} \end{aligned} \tag{11}$$

where

$g_{j=0...2}$	nearest neighbor resampled pixel values;
ϕ_s	sample-scene phase ($0 \le \phi_s < \Delta x_s$);
Δx_s	sample interval (sensed digital image pixel dimension);
Δx_s	$w_{\text{nadir}} i$;
w_{nadir}	nadir observation dimension;
i	positive integer;
$k1, k2$	values either side of the contrast edge ($k2 > k1$).

C. Probability of a Pixel Value over a High Contrast Edge Located in a Single Orbit of Nearest Neighbor Resampled Geometrically Correct Data

The probability distribution of a nearest neighbor resampled geometrically correct pixel value at a fixed location over the contrast edge is defined (12). The misalignment of the satellite data is modeled as a shift from the correct position that the data would be sensed at if there were no geolocation errors and is characterized by a geolocation error probability distribution

$$\begin{aligned} P(g_0)|_{x=a} &= \int_{-\infty}^{z - \frac{\Delta x_s}{2} - a} P_e(x)\, dx \\ P(g_1)|_{x=a} &= \int_{z - \frac{\Delta x_s}{2} - a}^{z + \frac{\Delta x_s}{2} - a} P_e(x)\, dx \\ P(g_2)|_{x=a} &= \int_{z + \frac{\Delta x_s}{2} - a}^{\infty} P_e(x)\, dx \\ & z = \phi_s \quad \text{when } 0 \le \phi_s < \frac{\Delta x_s}{x} \\ & z = \phi_s - \Delta x_s \quad \text{otherwise} \end{aligned} \tag{12}$$

where

$P(g_{j=0...2})\|_{x=a}$	probability distribution of nearest neighbor resampled geometrically corrected pixel values at fixed location $x = a$;
$P_e(x)$	geolocation error probability distribution describing the probability of x axis geolocation errors;
$g_{j=0...2}$	possible nearest neighbor resampled pixel values (11);
ϕ_s	sample-scene phase ($0 \le \phi_s < \Delta x_s$);
Δx_s	sample interval (sensed digital image pixel dimension);
Δx_s	$w_{\text{nadir}} i$;
w_{nadir}	nadir observation dimension;
i	positive integer;

D. Probability of a Pixel Value over a High Contrast Edge Located in a Minimum or Maximum Value Composite

If the probability distribution of a sample is identical and independent for successive samples, then the probability distributions of the minimum and maximum sample values are defined by order statistics as

$$\begin{aligned} P_{\min}(g) &= n(1 - A(g))^{n-1} P(g) \\ P_{\max}(g) &= n A(g)^{n-1} P(g) \\ & \text{where } A(g) = \int_{-\infty}^{g} P(g)\, dg \end{aligned} \tag{13}$$

where

g	sample value;
$P_{\min}(g)$	minimum sample value probability distribution;
$P_{\max}(g)$	maximum sample value probability distribution;
$P(g)$	sample value probability distribution;
n	number of samples.

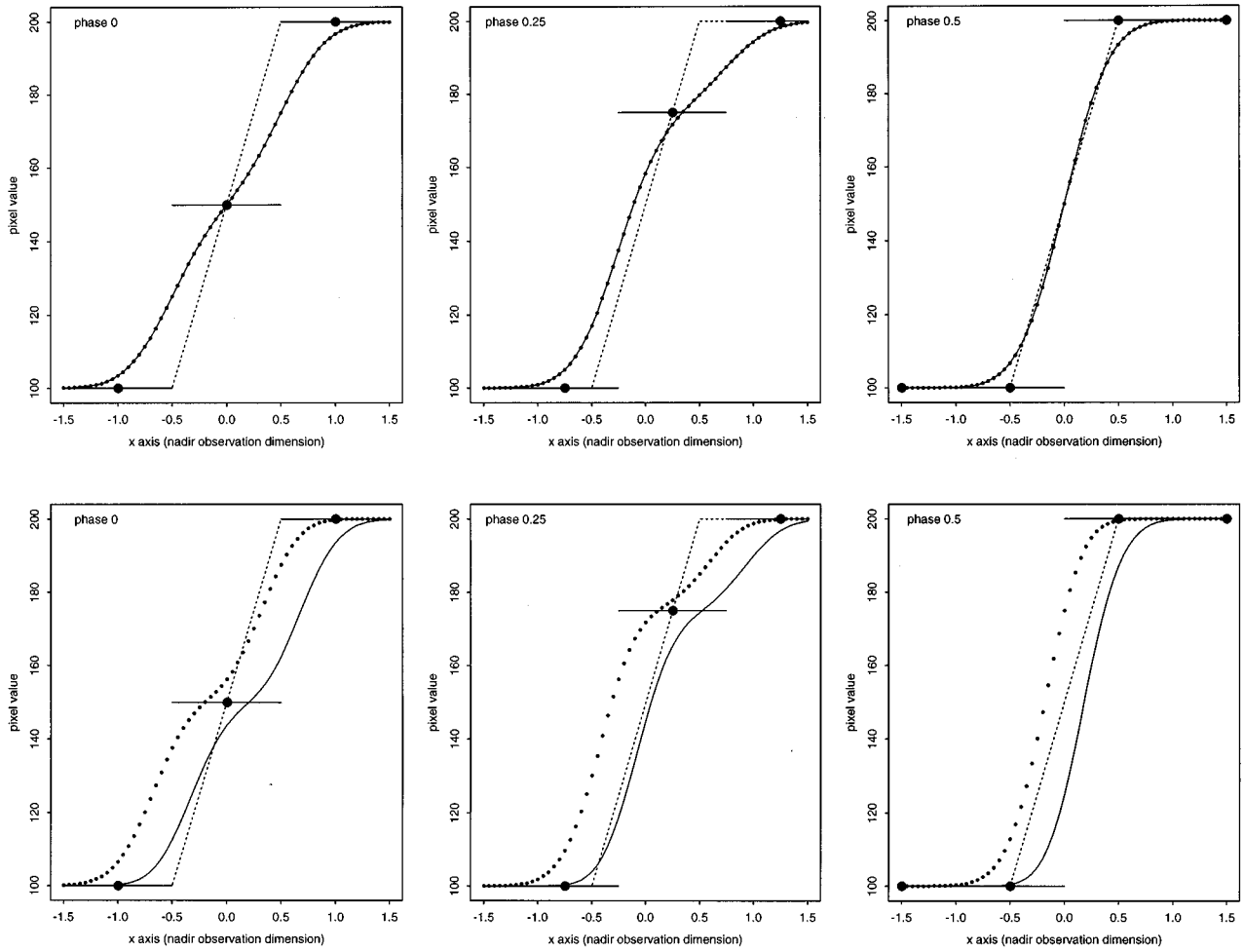

Fig. 4. Expected minimum value composited pixel values (solid curve) and expected maximum value composited pixel values (small solid dots) found after compositing a single orbit (top row) and two orbits (bottom row) of nearest neighbor resampled satellite data, illustrated for the nadir imaging cases shown in the top row of Fig. 3. The geolocation error is normally distributed with a mean of zero and σ equal to one third the nadir observation dimension.

This may be written in discrete form as

$$P_{\min}(g_j) = \sum_{i=0}^{n-1} \binom{n}{n-i} (1 - A(g_j))^i P(g_j)^{n-i}$$

$$P_{\max}(g_j) = \sum_{i=0}^{n-1} \binom{n}{n-i} (A(g_j) - P(g_j))^i P(g_j)^{n-i}$$

where $\binom{n}{n-i} = \frac{n!}{i!(n-i)!}$ and

$$A(g_{j=0\ldots m}) = \sum_{i=0}^{j} P(g_i) \quad (14)$$

where

g_j	sample value;
$P_{\min}(g_j)$	Minimum sample value probability distribution;
$P_{\max}(g_j)$	maximum sample value probability distribution;
$P = (g_{j=0}\ldots m)$	sample value probability distribution;
$m+1$	number of unique sample values;
n	number of samples.

Substitution of (12) into (14) gives the probability distribution of a pixel value at a fixed location over a high contrast edge in a minimum or maximum value composite. Application of (14) is invalid if the composited pixel values found in each orbit have different and/or dependent probability distributions. Although independence is assumed, the probability distributions are likely to be different when the observations are sensed with different view zenith angles and/or sample-scene phases. In these cases, an exhaustive comparison of the different probability distributions must be performed. This is computationally expensive because, although the order of compositing is unimportant, different orbits may be sensed with the same view zenith angle and sample-scene phase. The number of ways that a sample of r elements may be selected from a set of m cases when the order is unimportant and repetition is allowed increases rapidly with r as

$$C^R(m,r) = \frac{(m+r-1)!}{r!(m-1)!} \quad \text{where}$$

$$C^R(m,r) = r\text{-combination with replacement.} \quad (15)$$

For example, modeling eight composited orbits sensed with the same observation dimensions and with any of ten sample-scene

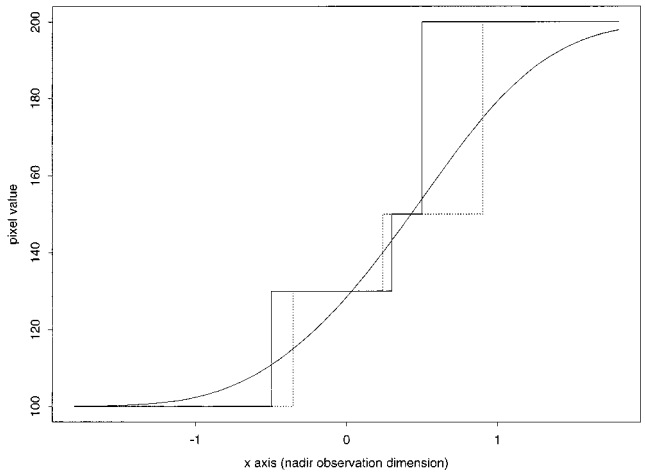

Fig. 5. Expected minimum composited pixel values found after compositing two orbits of nearest neighbor resampled satellite data over a hypothetical high contrast edge located at $x = 0$. The orbits are modeled as being sensed with the same nadir observation dimension and with sample-scene phases of 0.0 and 0.8. The geolocation error is normally distributed with a mean of zero and σ equal to half the nadir observation dimension. The perfectly registered expected composited pixel values (solid step), the misregistered expected composited pixel values (solid curve), and the misregistered expected composited pixel values rounded to the closest perfectly registered expected values (dashed step) are shown. The vertical lines are drawn for illustrative purposes only.

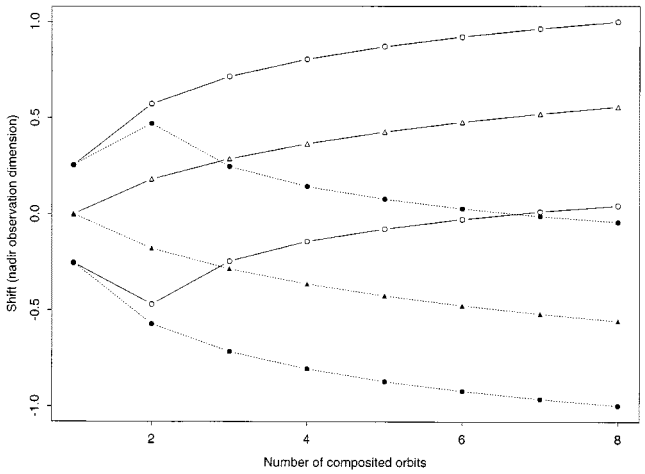

Fig. 6. Minimum, mean, and maximum shifts in the position of a composited high contrast edge after compositing one to eight misregistered orbits sensed at nadir. The shifts are calculated for every possible combination of ten sample-scene phases when the order is unimportant and repetition is allowed. A 3σ geolocation error equal to 1.8 the nadir observation dimension is modeled. Maximum value composited shifts are shown dashed, and minimum value composited shifts are shown solid. The mean shifts are denoted by triangles.

phases requires that $C^R(10, 8) = 24\,310$ sets of eight probability distributions must be compared. To similarly model the compositing of 32 orbits requires that more than 350 million sets of 32 probability distributions must be compared.

E. Shifts in the Position of a Composited High Contrast Edge due to Misregistration

Shifts in the position of a composited contrast edge feature due to misregistration are found by comparison of the expected pixel values when misregistered and perfectly registered orbits are composited. The shifts are derived by frequent comparison of these values across the contrast edge. The expected pixel values at a fixed location in a minimum and maximum value composite are defined as

$$\overline{g_{\min}} = \sum_{j=0}^{m} P_{\min}(g_j)(g_j)$$
$$\overline{g_{\max}} = \sum_{j=0}^{m} P_{\max}(g_j)(g_j) \tag{16}$$

where

$\overline{g_{\min}}$	expected minimum sample value;
$\overline{g_{\max}}$	expected maximum sample value;
$P_{\min}(g_{j=0\ldots m})$	minimum sample value probability distribution;
$P_{\max}(g_{j=0\ldots m})$	maximum sample value probability distribution;
$m+1$	number of unique sample values.

The expected misregistered pixel values are rounded to the closest perfectly registered values to enable their comparison. Comparisons are performed at intervals of one thousandth of the nadir observation dimension across the contrast edge and any shifts between the perfectly registered and misregistered edge profiles are derived. The shifts may or may not be observed in composited misregistered data depending upon the location of the geometrically correct pixel centers.

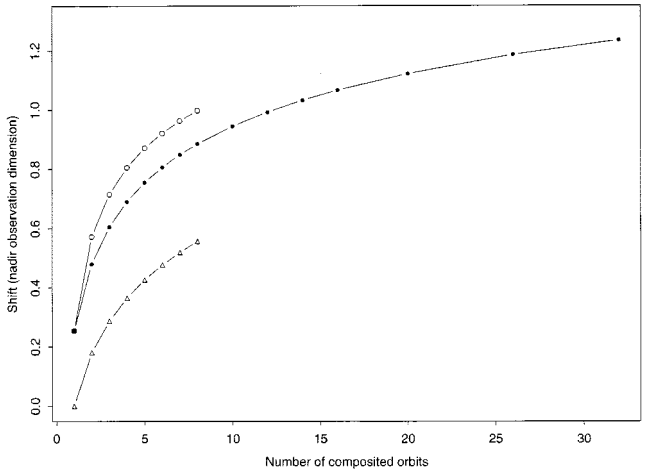

Fig. 7. Maximum shifts in the position of a composited high contrast edge after compositing one to 32 misregistered orbits sensed at nadir. The shifts are calculated using the conservative approximation (see text for details). A 3σ geolocation error equal to 1.8 the nadir observation dimension is modeled. The mean shifts (triangles) and the maximum shifts (clear circles) illustrated in Fig. 6 are superimposed for comparative purposes.

VI. Illustrative Modeling

Fig. 3 shows the optical image, the digital image and the nearest neighbor resampled image of a hypothetical contrast edge. Nadir, off-nadir, and far off-nadir imaging cases are shown where the observation dimension and sample interval are one, two, and three times the nadir observation dimension respectively. In each case the optical image smoothes the contrast edge over the observation dimension. Sample-scene phases of 0.0, 0.25 and 0.5 the observation dimension are illustrated. The position and values of the digital and nearest neighbor resampled

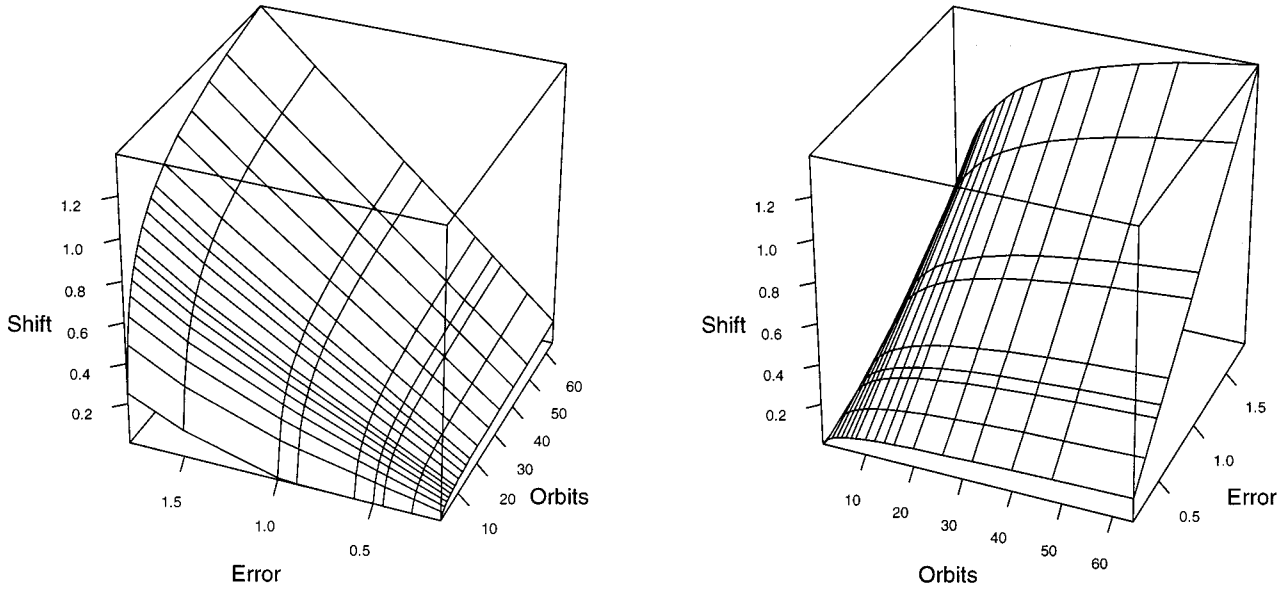

Fig. 8. Maximum shifts in the position of a high contrast edge feature after compositing different numbers of misregistered orbits of nearest neighbor resampled satellite data. Shifts are calculated assuming the conservative approximation (see text for detail) and are expressed as a fraction of the nadir observation dimension. Misregistration errors are defined by a zero-mean normal distribution with a 3σ error expressed in terms of the nadir observation dimension. Each orbit of satellite data is assumed to be sensed at nadir.

images are controlled by the sample-scene phase. Only when the sample-scene phase is zero or equal to half the observation dimension are the digital image and the resampled image values symmetrical about the edge. The geometrically correct image is not illustrated but would be defined by all or a subset of the nearest neighbor resampled image pixel values depending upon the locations of the geometrically correct pixel centers. Fig. 3 illustrates how a high contrast edge may be shifted in a nearest neighbor resampled geometrically correct image and how it may be broadened if the observations are sensed at greater view zenith angles.

Fig. 4 illustrates expected pixel values found after compositing misregistered satellite data sensed at nadir. The expected pixel values found after compositing one and two orbits of data are shown. When one orbit is composited the expected values are the same for minimum and maximum value compositing. When two orbits are composited the expected maximum value composited pixel values are shifted towards the lower valued side of the edge and the expected minimum value composited pixel values are shifted towards the higher valued side of the edge. This is in accordance with previously reported observations, for example, that maximum NDVI compositing enlarges vegetation boundaries, and is observed in Fig. 2.

Fig. 5 illustrates how shifts in the position of a contrast edge due to compositing misregistered data are quantified. The expected composited pixel values found after minimum value compositing two perfectly registered orbits of data and two misregistered versions are illustrated. The two orbits are modeled as being sensed with the same nadir observation dimensions and with different sample-scene phases. The misregistered expected composited pixel values rounded to the closest perfectly registered values are shown. The rounded misregistered expected composited pixel values (dashed step) are a shifted version of the perfectly registered values (solid step). The relative degree and direction of shifting is found by comparison of these edge profiles at intervals of one thousandth of the nadir observation dimension across the contrast edge. In this example shifts of 0.14, −0.06, and 0.40 the nadir observation dimension are found.

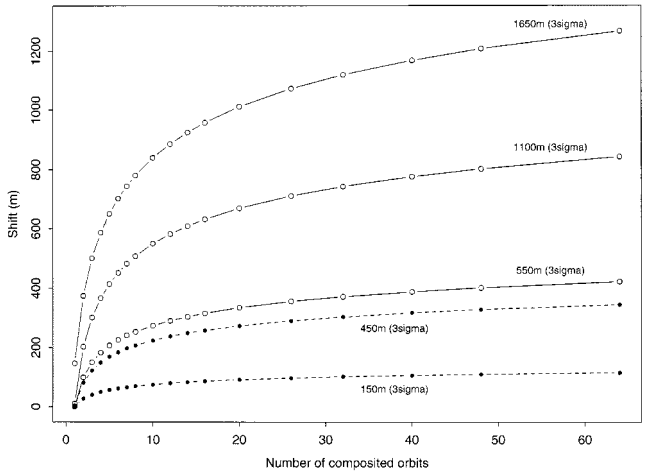

Fig. 9. Maximum shifts in the position of a composited high contrast edge plotted as a function of the number of composited orbits. Results are shown for 3σ geolocation errors of 550 m, 1100 m, and 1650 m, corresponding to 0.5, 1.0 and 1.5 a AVHRR 1.1 km nadir observation dimension, and for 3σ, geolocation errors of 450 m and 150 m corresponding to the MODIS geolocation design specification and operational geolocation goal, respectively. The composited orbits are assumed to be sensed at nadir. The conservative approximation is used (see text for details).

VII. AVHRR AND MODIS SIMULATIONS

Computational simulations are performed for a range of typical AVHRR and MODIS geolocation accuracies, compositing periods, and for different sample-scene phases and view zenith

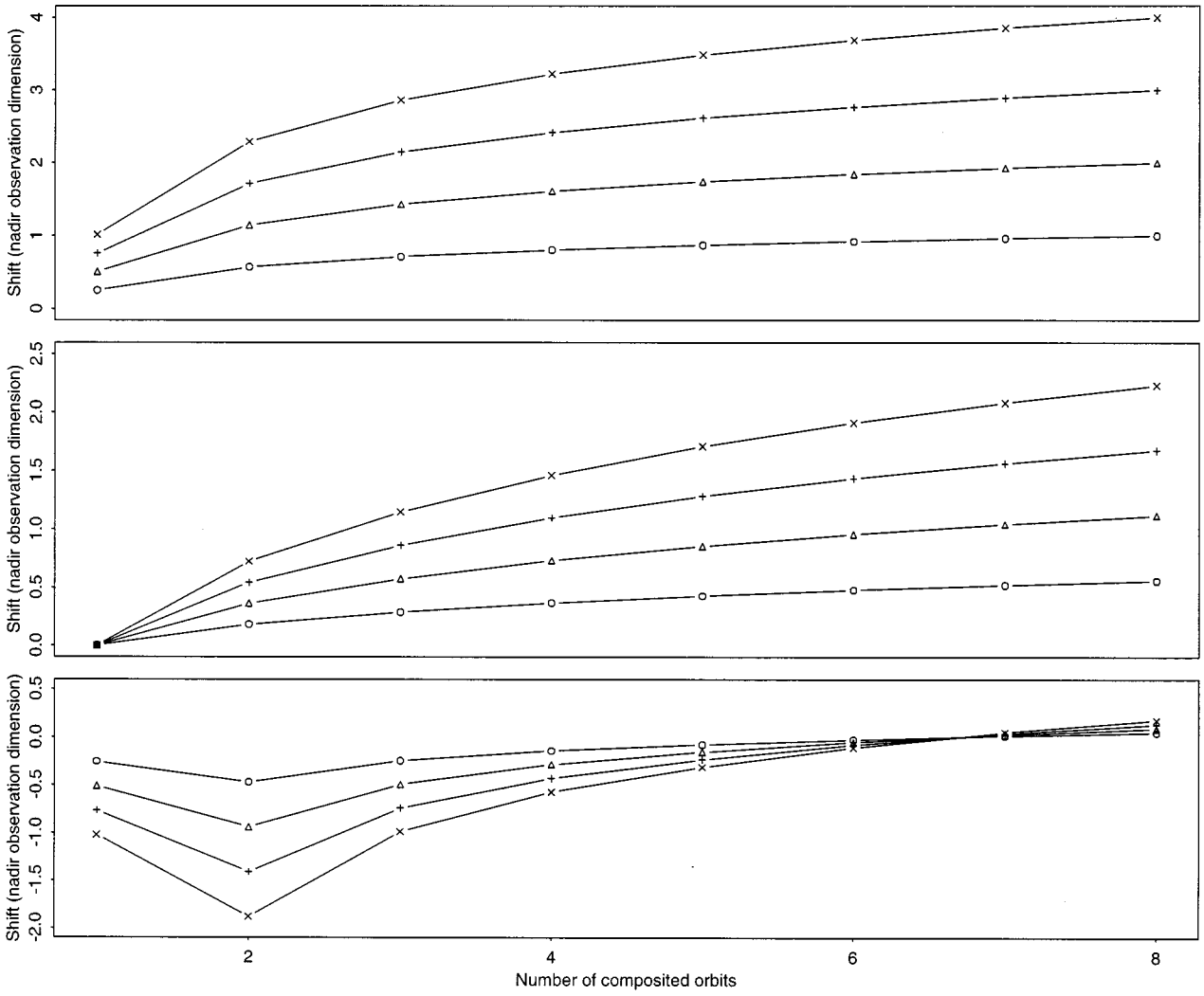

Fig. 10. (Top) Maximum; (middle) mean, and (bottom) minimum shifts in the position of a composited high contrast edge after compositing one to eight misregistered orbits. The shifts are shown for composites produced from observations all sensed with view zenith angles of 0° (circles), 46° (triangles), 57° (vertical crosses), or 63° (diagonal crosses). The shifts are calculated for all the different possible combinations of ten sample-scene phases when the order is unimportant and repetition is allowed. A 3σ geolocation error equal to 1.8 the sensed observation dimension is modeled.

angles. Each orbit of satellite data is modeled with an identical and independent normal geolocation error probability distribution with a mean of zero and a prespecified standard deviation (σ). Ten sample-scene phases are modeled with phases of 0.0, 0.1, 0.2, 0.3, 0.4, 0.5, 0.6, 0.7, 0.8, and 0.9 the local observation dimension. In this way, a high contrast edge found after compositing orbits sensed with different sample-scene phases may be defined with nearest neighbor values quantized at every tenth of the edge pixel value range. Shifts in the position of the edge corresponding to a tenth of the edge pixel value range may then be quantified.

A. AVHRR and MODIS Spatial Sensing Characteristics

The AVHRR sensor acquires earth observations over a field of view of approximately 110° and is carried onboard the NOAA satellites with a mean orbital period of 102 min and a repeat cycle of approximately nine days [47]. AVHRR data are available as local area coverage (LAC) data with a nadir observation dimension of approximately 1.1 km and as spatially averaged global area coverage (GAC) data. AVHRR LAC geolocation accuracies vary according to the geolocation methodology but are typically no better than the AVHRR observation dimension, although higher accuracies are possible [39], [48]. Lower geolocation accuracies may be obtained in regions where there are no apparent GCP's and because of the presence of clouds. AVHRR GAC values are computed by averaging four out of five consecutive observations for every third LAC scanline. AVHRR GAC simulations are not performed because of this nonlinear mixing. Global and continental scale maximum NDVI composited data sets have been produced using weekly, ten day, 15 day, and monthly compositing periods [49].

MODIS acquires earth observations over a field of view of approximately 110° in 36 spectral bands: 29 with 1 km at nadir observation dimensions, five with 500 m at nadir observation dimensions, and two with 250 m at nadir observation dimensions [2]. MODIS orbits the earth on the polar orbiting Earth observation system (EOS) with a mean period of 98.9 min and a repeat cycle of 16 days [50]. The MODIS geolocation design specification is 450 m (3σ) with an operational goal of 150 m (3σ) to be achieved after postprocessing using GCP's [45], [51]. Standard

MODIS land products are produced with 250 m, 500 m, and 1 km pixel dimensions using compositing periods of 8, 16, and 32 days [20].

B. Simulation Results

Fig. 6 illustrates the minimum, mean, and maximum shifts found after compositing one to eight misregistered orbits sensed at nadir. The shifts are calculated for every possible combination of the ten sample-scene phases when the order is unimportant and repetition is allowed (15). In general, the degree of shifting increases as more orbits are composited. The maximum value compositing shifts are predominantly towards the lower valued side of the feature (the mean and maximum shifts are always negative). Shifts towards the higher valued side of the contrast edge occur only infrequently and only when a small number of orbits are composited. The shifts are the same for minimum value compositing but occur in the opposite direction. Simulation of greater numbers of orbits than those illustrated in Fig. 6 rapidly becomes computationally prohibitive. Instead, a computationally efficient approximation is made. Shifts are calculated assuming that for a given number of composited orbits all the observations have the same sample-scene phase. This is repeated as many times as there are different sample-scene phases and the maximum shift is taken. Fig. 7 illustrates the results of this approximation for minimum or maximum value compositing one to 32 orbits and modeling the ten sample scene-phases. The mean and maximum shifts shown in Fig. 6 are superimposed for comparative purposes. It is evident that the approximation is a conservative estimate of the maximum shift derived by comparison of every sample-scene phase combination.

Fig. 8 illustrates the maximum shifts calculated for a range of geolocation errors and compositing periods assuming that all the observations are sensed at nadir. The computationally efficient modeling approach is used so that the results are conservative estimates. The degree of shifting is a linear function of the geolocation error and is related to the number of composited orbits in an inverse exponential manner. Fig. 9 illustrates these results in the context of AVHRR and MODIS data. Operational AVHRR geolocation accuracies are typically no better than plus or minus the nadir observation dimension. Equating this with a 1100 m 3σ geolocation error implies that high contrast edges may be shifted by approximately 550 m and by 740 m in AVHRR composites produced using ten and 32 nadir observations, respectively. By comparison, shifts of approximately 225 m and 300 m occur after compositing ten and 32 MODIS observations geolocated to the MODIS design specification (450 m, 3σ). These shifts decrease by a factor of three if the observations are geolocated to the MODIS operational goal (150 m, 3σ). This finding implies that the MODIS 250 m and 500 m observations should be geolocated to the MODIS operational goal before they can be used for reliable pixel-level change detection.

Except near the poles, the surface sensed by wide field of view polar orbiting sensors is sensed with different view zenith angles over the sensor repeat cycle. To simulate more realistic compositing the shifts found when misregistered observations are sensed with the same and different view zenith angles are investigated. Observations sensed with along scan observation dimensions one, two, three, and four times the nadir observation dimension are modeled. These correspond approximately to MODIS and AVHRR view zenith angles of 0° (nadir), 46°, 57°, and 63° (far-off nadir). In the along-track direction, MODIS and AVHRR observation dimensions are only twice as large as the nadir observation dimension at the extreme edge of the swath. Consequently, the shifts calculated for the 57° and 63° imaging cases will not occur in the along-track direction. Fig. 10 shows summary statistics of the shifts derived when composited observations are sensed with the same 0°, 46°, 57°, or 63° view zenith angle. Fig. 11 shows summary statistics calculated for the different possible ways of compositing the four view zenith angle cases. The shifts are derived by comparison of every possible combination of the ten sample-scene phases when the order is unimportant and repetition is allowed (15). In Fig. 10 the shifts associated with non-nadir imaging follow the same pattern as the nadir imaging shifts but are proportionally greater in magnitude according to the relative observation dimensions. For example, if the misregistered observations are sensed with 63° view zenith angles then the observation dimensions and shifts are four times greater than when the same number of nadir observations are composited. The maximum shifts illustrated in Fig. 11 are even greater and occur when the composited observations are sensed at nadir (0°) and far off-nadir (63°). These results imply that shifts of more than four and two times those illustrated in Figs. 8 and 9 may occur in composited AVHRR or MODIS data in the along scan and along-track directions respectively.

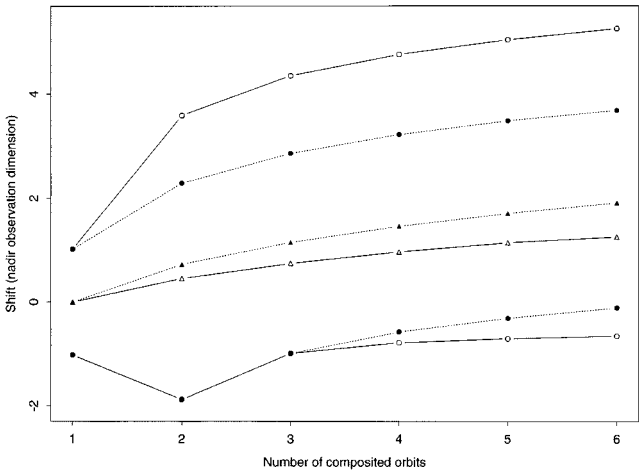

Fig. 11. Minimum, mean, and maximum shifts in the position of a composited high contrast edge after compositing one to six misregistered orbits. The solid lines show summary statistics calculated for all the different possible ways of compositing ten sample-scene phases and four view zenith angles (0°, 46°, 57°, and 63°) when the order is unimportant and repetition is allowed. The dashed lines illustrate the shifts found when only far off-nadir (63°) observations are composited (shown for comparative purposes). A 3σ geolocation error equal to 1.8 the sensed observation dimension is modeled.

VIII. Implications for Change Detection

The findings of this paper have implications for change detection capabilities when composited data are used. Before considering these, detection limitations imposed by the properties of the sensing system are considered for different types of change.

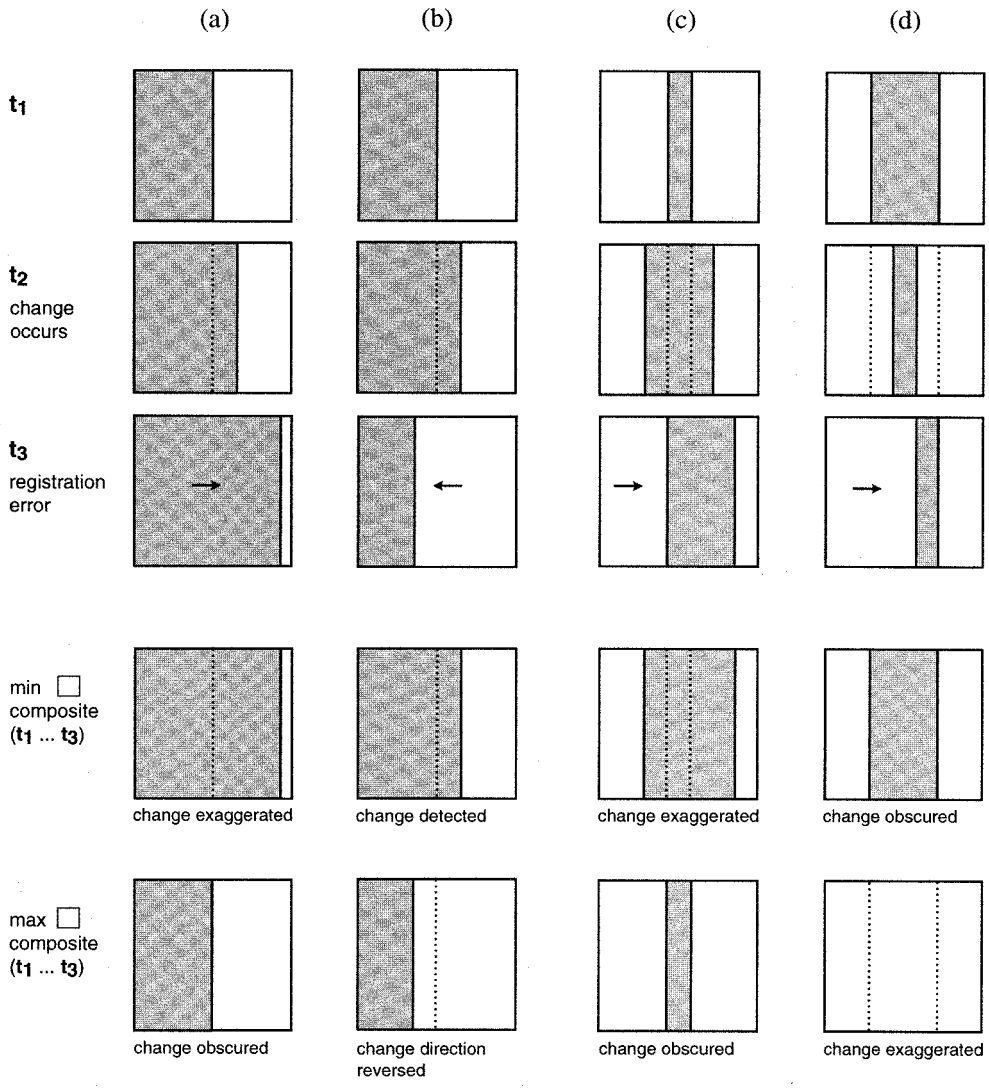

Fig. 12. Types of spatial change and the impact of misregistration errors upon minimum and maximum value composites.

Change processes introduce or move boundaries in remotely sensed data except when they cause a uniform increase or decrease in the emitted or reflected radiation. Detection of changes in the location of high contrast boundaries is limited primarily by the precision of geometric registration if the boundaries are straight and separate regions that are large relative to the pixel size [17]. Changes manifested by such boundaries are often anthropogenic, e.g., forest clear-cutting, agricultural cropping, or urban development. Boundaries that are not straight and/or that separate regions that are small relative to the pixel size cannot be easily located to subpixel accuracy. Consequently, their change detection is limited by both the spatial resolution (acquisition point spread function) and the geometric registration precision [17]. These types of change are manifested by many natural processes that occur under heterogeneous environmental conditions, for example, vegetation growth and senescence, action of insects, fire, and grazing. Detection of changes that have no spatial variation, e.g. growth of homogeneous vegetation covering many pixels, is limited by the radiometric sensitivity of the sensing system [17]. When composited data are used change detection capabilities may be reduced by additional limitations. This paper has shown that high contrast boundaries may be shifted when misregistered data are composited. Because these shifts are systematically towards the lower or higher valued side of the boundary they may exaggerate, reverse, or obscure change phenomena. Sub-pixel boundary location may also be less accurate because adjacent pixels may have been selected from different images sensed over the compositing period [24].

The ability to detect changes in high contrast boundary locations using composited data is dependent upon the compositing criterion and the relative directions of the change and any misregistration errors. This is illustrated in Fig 12. Changes that occur within a compositing period are obscured if the compositing procedure preferentially selects unchanged over changed pixels. If the misregistration error is in the same direction as the change [Fig. 12(a)], then the change will either be exaggerated by the misregistration error or will be obscured depending upon the compositing criterion. If the misregistration error is in the opposite direction to the change [Fig. 12(b)] then the change will be detected successfully or, if the misregistration error is greater than twice the change magnitude, the change direction reversed. Similar constraints

impact the ability to detect changes in features bounded by more than one high contrast boundary [Fig. 12(c) and (d)]. Changes of this sort include growth or shrinkage of point-like and irregularly shaped features (e.g., overgrazing around a well in semi-arid topical grasslands, development of burned areas) and changes in the small-axis dimension of linear features (e.g., certain types of forest clearance associated with agricultural development). If the feature boundaries change in opposing directions then the change will either be exaggerated by the misregistration error or will be obscured. Features that are evident in individual orbits may disappear in composited data if the magnitude and direction of the misregistration error is greater than the feature's small-axis dimension. This may preclude the detection of small and fragmented features and imposes a lower size limit on change detection capabilities commensurate with twice the misregistration error.

The effects described above may significantly bias area estimates made from composited satellite data and may be propagated into rates of change of location and area estimated from time series of composited data. These biases may have severe implications for applications that utilize such estimates. For example, the area of biomass burned may be estimated from composited data and is an important variable required to estimate trace gas and particulate emissions [27], [28].

IX. Concluding Remarks

The impact of misregistration upon compositing has been investigated using one-dimensional (1-D) models of the satellite imaging and geometric registration processes for a heterogeneous scene modeled by a high contrast edge such as a land cover interface. The position of such features has been shown to be shifted towards the lower and higher valued side of the feature in maximum and minimum value composites respectively when misregistered data are composited. Because the shifts are non-random they may systematically bias assessments made using composited data at local and global scales. The shifts are likely to bias estimates of location and area. They may also cause small and/or fragmented features that are evident in individual orbits to disappear in composited data precluding the ability to map such features or to detect their occurrence under a change detection scheme. When composited data are used for change detection the requirement for accurate geometric registration is higher than that required for the registration of individual satellite images e.g., [13], [14].

The results of AVHRR and MODIS simulations described in this study indicate that high contrast edges will be commonly shifted in composited data by half the nadir observation dimension (usually comparable to the geometrically correct pixel dimension) and may be shifted by several times this dimension. This has serious implications for applications that use individual AVHRR or MODIS composites (e.g., to estimate forest area) and that use time series of composites under a change detection scheme (e.g., to estimate rates of deforestation or to detect the occurrence of change). The degree of shifting increases with the geolocation error, the number of orbits that are composited, and when the composited observations are sensed with greater view zenith angles. Using precisely registered near-nadir observations and shorter compositing periods will cause the least amount of shifting. The findings of this study imply that the widely used maximum NDVI compositing procedure may be particularly sensitive to data misregistration as maximum NDVI compositing has been shown to preferentially select off-nadir observations [29], [52]. The results also imply that composited global data sets may contain larger misregistration impacts further polewards as more observations of the surface occur per day.

The AVHRR and MODIS simulation results may be used to infer the approximate geometric registration accuracy, view zenith angle threshold, and number of orbits required to produce composites suitable for change detection and other applications where shifts in the position of distinct features should be minimized. Further research is required, however, before a rigorous assessment of the optimal mix of these parameters may be made. This research should include models of the likely cloud and atmospheric contamination, the rates of change of the terrestrial features of interest, and more specific modeling of the sensor imaging characteristics than described in this study. In general, it is recommended that efforts are made to improve the geometric registration accuracy and that high view zenith angle observations are rejected before reducing the number of composited orbits. This is because the compositing period should be sufficiently long to ensure selection of near-nadir, cloud free, atmospherically uncontaminated observations [5]. If the geometric registration accuracy can be improved, for example, by use of ground control points, then the cost-benefit of different levels of geometric improvement can be inferred by examination of the results described in this study. Similarly, the benefits of rejecting high view zenith angles may be assessed against factors such as the reduction in the sensed area. Another approach to reduce the impact of misregistration on composited data is to composite observations sensed by independent satellite systems. Using different satellite data would increase the number of observations of the surface and provide the opportunity to reject poorly geolocated orbits and observations sensed at high view zenith angles. This approach has particular potential for the MODIS instrument scheduled for launch onboard two satellites to provide morning and evening global observations in 2000 and afternoon and night observations in 2001.

Acknowledgment

The author wishes to thank L. Giglio, R. Wolfe, X. Zhan, and J. Townshend for helpful comments on this manuscript.

References

[1] Y. Kaufman, "The atmospheric effects on remote sensing and its correction," in *Theory and Applications of Optical Remote Sensing*, G. Asar, Ed. New York: Wiley, 1989, pp. 336–428.

[2] R. E. Wolfe, D. P. Roy, and E. Vermote, "The MODIS land data storage, gridding and compositing methodology: L2 grid," *IEEE Trans. Geosci. Remote Sensing*, vol. 36, pp. 1324–1338, July 1998.

[3] B. Pinty and M. Verstraete, "On the design and validation of surface bidirectional reflectance and albedo models," *Remote Sens. Environ.*, vol. 41, pp. 155–167, 1992.

[4] H. Rahman, "Atmospheric optical depth and water vapour effects on the angular characteristics of surface reflectance in NOAA AVHRR," *Int. J. Remote Sensing*, vol. 17, pp. 2981–2999, 1996.

[5] B. Holben, "Characteristics of maximum-value composite images from temporal AVHRR data," *Int. J. Remote Sensing*, vol. 7, pp. 1417–1434, 1986.

[6] R. DeFries, M. Hansen, and J. Townshend, "Global discrimination of land cover types from metrics derived from AVHRR pathfinder data," *Remote Sens. Environ.*, vol. 54, pp. 209–222, 1995.
[7] T. R. Loveland and A. S. Belward, "The IGBP-DIS global 1 km land cover data set, discover: First results," *Int. J. Remote Sensing*, vol. 18, pp. 3291–3295, 1997.
[8] E. F. Lambin and A. H. Strahler, "Change-vector analysis in multi-temporal space—A tool to detect and categorize land-cover change processes using high temporal-resolution satellite data," *Remote Sens. Environ.*, vol. 48, pp. 231–244, 1994.
[9] X. Zhan, R. DeFries, J. R. G. Townshend, C. DiMiceli, M. Hansen, C. Huang, and R. Sohlberg, "The 250 m global land cover change product from the moderate resolution imaging spectroradiometer of NASA's earth observing system," *Int. J. Remote Sensing*, vol. 21, pp. 1433–1460, 2000.
[10] P. J. Sellers, S. O. Los, C. J. Tucker, C. O. Justice, D. A. Dazlich, G. J. Collatz, and D. A. Randall, "A revised land surface parameterization (SiB_2) for atmospheric GCMs. 2. The generation of global fields of terrestrial biophysical parameters from satellite data," *J. Climate*, vol. 9, pp. 706–737, 1996.
[11] S. O. Los, "Linkages between global vegetation and climate—An analysis based on NOAA advance very high resolution radiometer data," Ph.D. Thesis, NASA Goddard Space Flight Center, Greenbelt, MD, 1998.
[12] F. C. Billingsley, "Modeling misregistration and related effects on multispectral classification," *Photogramm. Eng. Remote Sensing*, vol. 48, pp. 421–430, 1982.
[13] J. R. G. Townshend, C. O. Justice, C. Gurney, and J. McManus, "The impact of misregistration on change detection," *IEEE Transactions Geosci. Remote Sensing*, vol. 30, pp. 1054–1060, Sept. 1992.
[14] X. Dai and S. Khorram, "The effects of image misregistration on the accuracy of remotely sensed change detection," *IEEE Trans. Geosci. Remote Sensing*, vol. 36, pp. 1566–1577, July 1998.
[15] A. Moody and A. Strahler, "Characteristics of composited AVHRR data and problems in their classification," *Int. J. Remote Sensing*, vol. 15, pp. 3473–3491, 1994.
[16] D. M. Stoms, M. J. Bueno, and F. W. David, "Viewing geometry of AVHRR image composites derived using multiple criteria," *Photogramm. Eng. Remote Sensing*, vol. 63, pp. 681–689, 1997.
[17] J. R. G. Townshend and C. O. Justice, "Selecting the spatial resolution of satellite sensors required for global monitoring of land transformations," *Int. J. Remote Sensing*, vol. 9, pp. 187–236, 1988.
[18] J. C. Eidenshink and J. L. Faundeen, "The 1 km AVHRR global land data set—1st stages in implementation," *Int. J. Remote Sensing*, vol. 15, pp. 3443–3462, 1994.
[19] N. Z. El Saleous, E. F. Vermote, C. O. Justice, J. R. G. Townshend, C. J. Tucker, and S. N. Goward, "Improvements in the global biospheric record from the advanced very high resolution radiometer (AVHRR)," *Int. J. Remote Sensing*, vol. 21, pp. 1251–1277, 2000.
[20] C. O. Justice, E. Vermote, J. Townshend, R. Defries, D. Roy, D. Hall, V. Salomonson, J. Privette, G. Riggs, A. Strahler, W. Lucht, R. Myneni, Y. Knyazikhin, S. Running, R. Nemani, Z. Wan, A. Huete, W. van Leeuwen, R. Wolfe, L. Giglio, J.-P. Muller, P. Lewis, and M. Barnsley, "The moderate resolution imaging spectroradiometer (MODIS): Land remote sensing for global change research," *IEEE Trans. Geosci. Remote Sensing*, vol. 36, pp. 1228–1249, July 1998.
[21] L. Wald, "Some terms of reference in data fusion," *IEEE Trans. Geosci. Remote Sensing*, vol. 37, pp. 1190–1193, May 1999.
[22] B. J. Choudhury, N. E. Digirolamo, and T. J. Dorman, "A comparison of reflectances and vegetation indices from three methods of compositing the AVHRR-GAC data over Northern Africa," *Remote Sensing Rev.*, vol. 10, pp. 245–263, 1994.
[23] J. Cihlar, D. Manak, and M. D'Iorio, "Evaluation of compositing algorithms for AVHRR data over land," *IEEE Trans. Geosci. Remote Sensing*, vol. 32, pp. 427–437, Mar. 1994.
[24] D. P. Roy, "Investigation of the maximum normalized difference vegetation index (NDVI) and the maximum surface temperature (T_s) AVHRR compositing procedures for the extraction of NDVI and T_s over forest," *Int. J. Remote Sensing*, vol. 18, pp. 2383–2401, 1997.
[25] J. Descloitres and E. Vermote, "Operational retrieval of the spectral surface reflectance and vegetation index at global scale from SeaWiFS data," in *Int. Conf. Aerosols, Radiation budget—Land Surfaces—Ocean Colour: The Contribution of POLDER and New Generation Spaceborne Sensors to Global Change Studies*, Meribel, France, Jan. 18–22, 1999.
[26] D. R. Cahoon, B. J. Stocks, J. S. Levine, W. R. Cofer, and J. M. Pierson, "Satellite analysis of the severe 1987 forest-fires in northern China and southeastern Siberia," *J. Geophys. Res.*, vol. 99, pp. 18627–18638, 1994.
[27] P. M. Barbosa, J. M. C. Pereira, and J. M. Gregoire, "Compositing criteria for burned area assessment using multi-temporal low resolution satellite data," *Remote Sens. Environ.*, vol. 65, pp. 38–49, 1998.
[28] D. P. Roy, L. Giglio, J. K. Kendall, and C. O. Justice, "Multi-temporal active-fire based burn scar detection algorithm," *Int. J. Remote Sensing*, vol. 20, pp. 1031–1038, 1999.
[29] D. Meyer, M. Verstraete, and B. Pinty, "The effect of surface anisotropy and viewing geometry on the estimation of NDVI from AVHRR," *Remote Sensing Rev.*, vol. 12, pp. 3–27, 1995.
[30] J. Cihlar, H. Ly, Z. Q. Li, J. Chen, H. Pokrant, and F. T. Huang, "Multi-temporal, multichannel AVHRR data sets for land biosphere studies—Artifacts and corrections," *Remote Sens. Environ.*, vol. 60, pp. 35–57, 1997.
[31] J. Price, "Land surface temperature measurements from the split window channels of the NOAA 7 advanced very high resolution radiometer," *J. Geophys. Res.*, vol. 89, pp. 7231–7237, 1984.
[32] A. K. Jain, *Fundamentals of Digital Image Processing*. Englewood Cliffs, NJ: Prentice-Hall, 1989.
[33] S. E. Reichenbach, D. E. Koehler, and D. W. Strelow, "Restoration and reconstruction of AVHRR images," *IEEE Trans. Geosci. Remote Sensing*, vol. 33, pp. 997–1007, July 1995.
[34] J. Settle and N. Campbell, "On the errors of two estimators of sub-pixel fractional cover when mixing is linear," *IEEE Trans. Geosci. Remote Sensing*, vol. 36, pp. 163–170, Jan. 1998.
[35] J. F. Moreno, S. Gandia, and J. Melia, "Geometric integration of NOAA AVHRR and SPOT data—Low resolution effective parameters from high-resolution data," *IEEE Trans. Geosci. Remote Sensing*, vol. 30, pp. 1006–1014, Sept. 1992.
[36] D. P. Roy, B. Devereux, B. Grainger, and S. White, "Parametric geometric correction of airborne thematic mapper imagery," *Int. J. Remote Sensing*, vol. 18, pp. 1865–1887, 1997.
[37] A. P. Cracknell and K. Paithoonwattanakij, "Pixel and sub-pixel accuracy in geometrical correction of AVHRR imagery," *Int. J. Remote Sensing*, vol. 10, pp. 661–667, 1989.
[38] F. S. Patt, R. H. Woodward, and W. W. Gregg, "An automated method for navigation assessment for Earth survey sensors using island targets," *Int. J. Remote Sensing*, vol. 18, pp. 3311–3336, 1997.
[39] J. F. Moreno and J. Melia, "A method for accurate geometric correction of NOAA AVHRR HRPT data," *IEEE Trans. Geosci. Remote Sensing*, vol. 31, pp. 204–226, Jan. 1993.
[40] G. Konecny, "Methods and possibilities for digital differential rectification," *Photogramm. Eng. Remote Sensing*, vol. 45, no. 6, pp. 727–734, 1979.
[41] S. K. Park and R. A. Schowengerdt, "Image reconstruction by parametric cubic convolution," *Comput. Vis., Graph., Image Processing*, vol. 23, pp. 258–272, 1983.
[42] S. Shlien, "Geometric correction, registration, and resampling of landsat imagery," *Can. J. Remote Sensing*, vol. 5, pp. 74–89, 1979.
[43] R. Pech and A. Davis, "Reflectance modeling of semiarid woodlands," *Remote Sens. Environ.*, vol. 23, pp. 365–377, 1987.
[44] B. Holben and Y. Shimabukuro, "Linear mixing model applied to coarse spatial resolution data from multispectral sensors," *Int. J. Remote Sensing*, vol. 14, pp. 2231–2240, 1993.
[45] M. Nishihama, R. Wolfe, D. Solomon, F. Patt, J. Blanchette, A. Fleig, and E. Masuoka, "MODIS Level 1A Earth Location Algorithm Theoretical Basis Document," Goddard Space Flight Center, Greenbelt, MD, NASA Tech. Memo., SDST-092, Version 3.0, Aug. 26, 1997.
[46] D. Baldwin and W. J. Emery, "Spacecraft attitude variations of NOAA-11 inferred from AVHRR imagery," *Int. J. Remote Sensing*, vol. 16, pp. 531–548, 1995.
[47] K. B. Kidwell, "NOAA Polar Orbiter Data User's Guide," National Climatic Data Center, Washington, DC, 1995.
[48] G. W. Rosborough, D. G. Baldwin, and W. J. Emery, "Precise AVHRR image navigation," *IEEE Trans. Geosci. Remote Sensing*, vol. 32, pp. 644–657, Mar. 1994.
[49] J. R. G. Townshend, "Global data sets for land applications from the AVHRR: An introduction," *Int. J. Remote Sensing*, vol. 15, pp. 3319–3332, 1994.
[50] V. V. Salomonson, W. L. Barnes, P. W. Maymon, H. E. Montgomery, and H. Ostrow, "MODIS: Advanced facility instrument for studies of the earth as a system," *IEEE Trans. Geosci. Remote Sensing*, vol. 27, pp. 145–153, Mar. 1989.
[51] R. E. Wolfe, M. Nishihama, A. J. Fleig, and D. P. Roy, "The MODIS operational geolocation error analysis and reduction methodology," in *Proc. IGARSS '99*, Hamburg, June 28–July 2 1999.
[52] Z. L. Zhu and L. Yang, "Characteristics of the 1 km AVHRR data set for North America," *Int. J. Remote Sensing*, vol. 17, pp. 1915–1924, 1996.

David P. Roy received the B.Sc. degree in geophysics from the University of Lancaster, Lancaster, U.K., in 1987, the M.Sc. degree in remote sensing and image processing technology from the University of Edinburgh, Edinburgh, U.K., in 1988, and the Ph.D. degree from the University of Cambridge, Cambridge, U.K., in 1993.

He was a Research Fellow with the U.K. National Environment Research Council for Thematic Information Systems, University of Reading, Reading, U.K. from 1993 to 1994, and from 1994 to 1996, he was with the Space Applications Institute of the Joint Research Center of the European Commission, Ispra, Italy. He is currently an Assistant Research Scientist with the Department of Geography, University of Maryland, College Park, working at NASA Goddard Space Flight Center, Greenbelt, MD. His research interests include the quality assurance/assessment of the EOS MODIS land products, forest mapping, and development of a MODIS burn scar product.